Pergamon

Int. Comm. Heat Mass Transfer, Vol. 29, No. 7, pp. 993-1003, 2002

0735–1933/02/$–see front matter

PII: S0735-1933(02)00419-0

LAMINAR NATURAL CONVECTION AROUND AN ISOTHERMAL SQUARE CYLINDER AT DIFFERENT ORIENTATIONS

Shohel Mahmud, Prodip Kumar Das, and Nasim Hyder
Department of Mechanical Engineering
Bangladesh University of Engineering and Technology (BUET)
Dhaka-1000, Bangladesh

(Communicated by J.P. Hartnett and W.J. Minkowycz)

ABSTRACT

Numerical simulation has been performed to predict the fluid flow and heat transfer characteristics around a square cylinder at different orientations. Finite volume method is used to discretize the governing equations. A body fitted grid with collocated variable arrangement is employed. System of equations are solved by Stone's SIP solver. Thermal field is presented in the form of isothermal lines. Heat transfer is presented in the form of Nusselt number for a range of Grashof numbers, $10 \leq Gr \leq 10^5$, and angular orientations, $0^0 \leq \theta \leq 90^0$. Skin friction and pressure coefficients are also presented. For a constant Grashof number, angular position 45^0 shows the maximum heat transfer rate compared to other angular positions. **© 2002 Elsevier Science Ltd**

Introduction

Heat transfer by natural convection from a horizontal cylinder in confined enclosures has various applications, ranging from heat exchangers to solar heating and cooling of electronic packages. Sathe *et al.* [1] presented an extensive study of air-cooled electronic packages in their review paper. They also focused on different aspect of geometrical configurations. Cylindrical bodies of different configurations are always paid attention for simplicity of their analyses. Many analytical, numerical, and experimental results are found in different references for circular and elliptical cylinder. Both of them have well defined geometry and mathematical equations that govern the contour of their perimeters. Flow and heat transfer patterns near the cylinders are greatly influenced by the shape of their cross-section. Several authors reported the natural convection from horizontal circular [2 – 4] and elliptical cylinder [8 – 10]. Square cylinders have also some applications though they are limited compared to the circular or elliptic cylinder. In our earlier work [5], we presented flow and heat transfer performance around an isothermal

square cylinder using rectangular mesh with inactive block-off region [6]. The block-off region shows some disadvantages during the application of boundary condition (isothermal and no-slip wall). The present work is an extension of our previous work [5]. The aim was to obtain a method with good accuracy, stability and convergence properties that can be used to predict buoyancy-induced flow and heat transfer around an isothermal square cylinder.

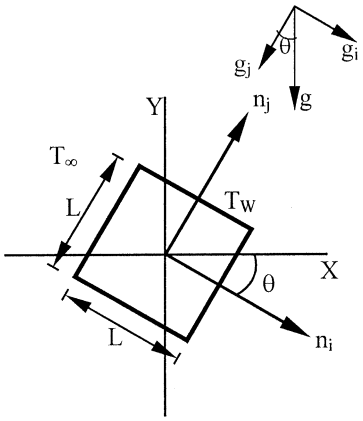

FIG. 1
Schematic diagram of the cylinder

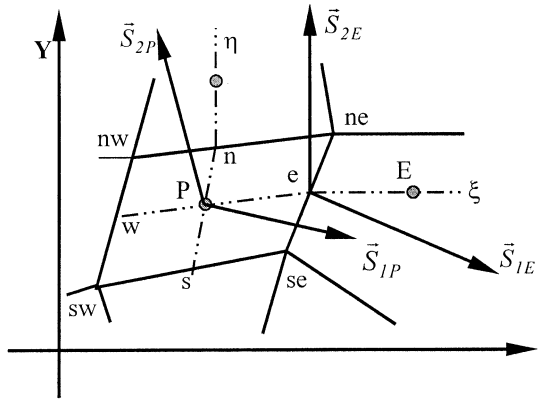

FIG. 2
An elementary control volume

Numerical Scheme

Fig. 1 shows the schematic diagram of the problem under consideration. Fig. 2 shows a typical CV of this mesh with different geometric notations. All CV's have the same notations. In the present study, two grid sizes (72×32 and 144×64) are selected. Results are presented only for fine the fine grid (144×64) solutions for better accuracy.

The primary variables are the Cartesian velocity components, pressure, and temperature. Density is linked to the temperature variation via Boussinesq approximation. Pressure-velocity coupling is achieved through SIMPLE algorithm. The discretization is carried out on control volumes defined by a boundary fitted, non-orthogonal grid. Since Cartesian based vectors are employed, the method is not sensitive to grid smoothness. The co-ordinate free integral forms of the steady state conservation equations for mass, momentum, and energy are as follows:

$$\int_S \rho \mathbf{v}.\mathbf{n}\, dS = 0 \qquad (1)$$

$$\int_S \rho u_i \mathbf{v}.\mathbf{n}\,\mathrm{d}S = \int_S \mu \,\mathrm{grad}\, u_i.\mathbf{n}\,\mathrm{d}S - \int_S p\mathbf{i}_i.\mathbf{n}\,\mathrm{d}S + \int_V \rho g_i \,\mathrm{d}V \tag{2}$$

$$\int_S \rho u_j \mathbf{v}.\mathbf{n}\,\mathrm{d}S = \int_S \mu \,\mathrm{grad}\, u_j.\mathbf{n}\,\mathrm{d}S - \int_S p\mathbf{i}_j.\mathbf{n}\,\mathrm{d}S + \int_V \rho g_j \,\mathrm{d}V \tag{3}$$

$$\int_S \rho T \mathbf{v}.\mathbf{n}\,\mathrm{d}S = \int_S \frac{\mu}{\mathrm{Pr}} \mathrm{grad}\, T.\mathbf{n}\,\mathrm{d}S \tag{4}$$

The Boussinesq approximation is:

$$\rho = \rho_0 g\beta(T - T_0) \tag{5}$$

The generalized form of Eqs. (1) – (4) is given in the following equation

$$\int_S \rho\phi \mathbf{v}.\mathbf{n}\,\mathrm{d}S = \int_S \Gamma \,\mathrm{grad}\,\phi.\mathbf{n}\,\mathrm{d}S + \int_V q_\phi \mathrm{d}V \tag{6}$$

Here S is the surface and V is the volume of the arbitrary control volume, $\mathbf{n}$ is the unit vector normal to S and directed outwards, $\mathbf{v}$ is the velocity vector, u_i and u_j are the Cartesian velocity components, ρ, μ, Pr, p, and T are the density, viscosity, Prandtl number, pressure, and temperature, respectively.

Discretization Method

The solution domain is subdivided into a finite number of contiguous quadrilateral control volumes (CV). The CVs are defined by coordinates of their vertices, which are assumed to be connected by straight lines. This simple form is possible due to the fact that the equations contain no curvature terms and only the projections of the CV faces onto Cartesian coordinates surfaces are required in the course of discretization, as demonstrated below. All the dependent variables solved for and all fluid properties are stored in the CV center (collocated arrangement). A suitable spatial distribution of dependent variables is assumed and the conservation Eqs. (1) – (4) are applied to each CV, leading to a system of non-linear algebraic equations. The main steps of discretization procedure to calculate convection and diffusion fluxes and source terms are outlined below.

The mass flux through the cell face 'e' (Fig. 2) is evaluated as

$$\dot{m}_e = \int_{S_e} \rho \mathrm{V}.\mathrm{dS} \approx (\rho \mathrm{V})_e.\mathbf{S}_{1e} = \rho_e \left(\mathrm{US}_1^{\mathrm{x}} + \mathrm{VS}_1^{\mathrm{y}}\right) \tag{7}$$

where $\mathbf{S}_{1e}$ is the surface vector representing the area of the cell face (ξ=const.) and $\mathrm{S}_{1e}^{\mathrm{x}}$ and $\mathrm{S}_{1e}^{\mathrm{y}}$ denotes its Cartesian components. These are given in terms of the CV vertex coordinates as follows:

$$S_{1e}^{x} = (y_n - y_s) \quad \text{and} \quad S_{1e}^{y} = -(x_n - x_s) \tag{8}$$

The mean cell face velocity components, U_e and V_e are obtained by interpolating neighbors' nodal values in a way which ensures the stability of grid scheme. The convection flux of any variable ϕ can now be expressed as:

$$F_e^C = \int_{S_e} \rho\phi V.dS \approx (\rho\phi V)_e . S_{1e} = \dot{m}_e \phi_e \tag{9}$$

The diffusion flux of ϕ is calculated as:

$$F_e^D = -\int_{S_e} \Gamma_\phi \text{grad}\,\phi.dS \approx -(\Gamma_\phi \text{grad}\phi)_e . S_{1e} \tag{10}$$

By expressing the gradient of ϕ at the cell face center 'e', which is taken here to represent the mean value over the whole cell face, through the derivatives in ξ and η directions (Fig. 2) and by discretizing these derivatives with CDS, the following expression results:

$$F_e^D \approx \frac{\Gamma_{\varphi,e}}{\mathbf{S_{1e}}.\mathbf{PE}} \left[(\phi_E - \phi_P)(\mathbf{S_{1e}}.\mathbf{S_{1e}}) + \underline{(\phi_n - \phi_s)_e (\mathbf{S_{1e}}.\mathbf{S_{2e}})} \right] \tag{11}$$

PE is the vector representing the distance from P to E, directed towards E. $\mathbf{S_{2e}}$ is the surface vector orthogonal to **PE** and directed outwards positive η coordinate (Fig. 2), representing the area in the surface η=0 bounded by P and E. Its x and y components are:

$$S_{2e}^{x} = -(y_E - y_P) \quad \text{and} \quad S_{2e}^{y} = (x_E - x_P) \tag{12}$$

The volumetric source term is integrated by simply multiplying the specific source at the control volume center P (which is assumed to represent the mean value over the whole cell) with the cell volume i.e.

$$Q_\phi^q = \int_V q_\phi dV \approx (q_\phi)_P \Delta V \tag{13}$$

The pressure term in the momentum equations are treated as body force and may be regarded as pressure sources for the Cartesian velocity components. They are evaluated as:

$$Q_{u_i}^p = -\int_S p\mathbf{i_i}.\mathbf{dS} = -\int_V (\text{grad}\, p.\mathbf{i_i})dV \approx -\left[(p_e - p_w)\mathbf{S_{1P}} + (p_n - p_s)\mathbf{S_{2p}} \right]\mathbf{i_i} \tag{14}$$

where the surface vectors $\mathbf{S_{1p}}$ and $\mathbf{S_{2p}}$ represent the area of the CV cross section at ξ=0 and η=0 respectively. Since CV's are bounded by straight lines, these two vectors can be expressed through the CV surface vectors, e.g. $\mathbf{S_{1P}}$=0.5($\mathbf{S_{1e}}$+ $\mathbf{S_{1w}}$). Terms in the momentum equations, not featuring in Eq. (6), are

discretized using the same approach and added to the source term. After summing up all cell face fluxes and sources, the discretized transport equation reduces to the following algebraic equation:

$$A_P\phi_P + \sum_{nb} A_{nb}\phi_{nb} = Q_\phi \tag{15}$$

where the coefficients, A_{nb}, contains the convective and diffusive flux contributions and Q_ϕ represents the source term. The system of equations is solved by using Stone's SIP solver. For details, see ref. [7].

Results and Discussions

At lower Gr, fluid near the cylinder wall is almost stagnant due to high viscous effect. Dominance of buoyant effect increases with the increase of Gr. Fluid motion is greatly affected by the orientation of the cylinder. At $\theta=0^0$, fluid is moving upwards along the two vertical walls. Fluid velocity is zero at the wall and at the tip of the boundary layer. Fluid over the top wall is always unstable (like Benard flow). Fluid from the side wall is mixed with the fluid at top wall and hence accelerated. Separation occurs at the middle of the top surface for $\theta=0^0$ and form the symmetrical edge (facing upwards) for $\theta=45^0$. For nonsymmetrical orientations, separation occurs from a point of the top surface that is closed to the top edge of the cylinder.

Isothermal lines are presented in Fig. 3 for three selected angular positions ($\theta=0^0$, 45^0, 60^0) and Grashof numbers ($Gr=10^3$, 10^4, 10^5). At lower Gr, conduction dominated isothermal lines are observed for each orientation. Upward velocity is almost negligible for high viscous force. Buoyant force starts to dominate with the increase of Gr. Isothermal lines are concentrated near the cylinder wall showing high temperature gradient as well as high heat transfer.

Heat transfer is presented by local and global values of Nusselt number. Figs. 4(a) – 4(d) show the local heat transfer distribution along the perimeter of the cylinder. For a particular angular position, profiles are similar in shape, only variation observed in magnitudes. Each corner shows high heat transfer due to the large temperature gradient normal to the surface. Effect of orientation of the cylinder on heat transfer is shown in Fig. 5. For a particular Gr, heat transfer is maximum at $\theta=45^0$ and this value increases with the increase of Gr. The projected area across the buoyant plume is maximum at this position showing maximum heat transfer rate. Fig. 6 shows the average heat transfer rate as a function of Gr.

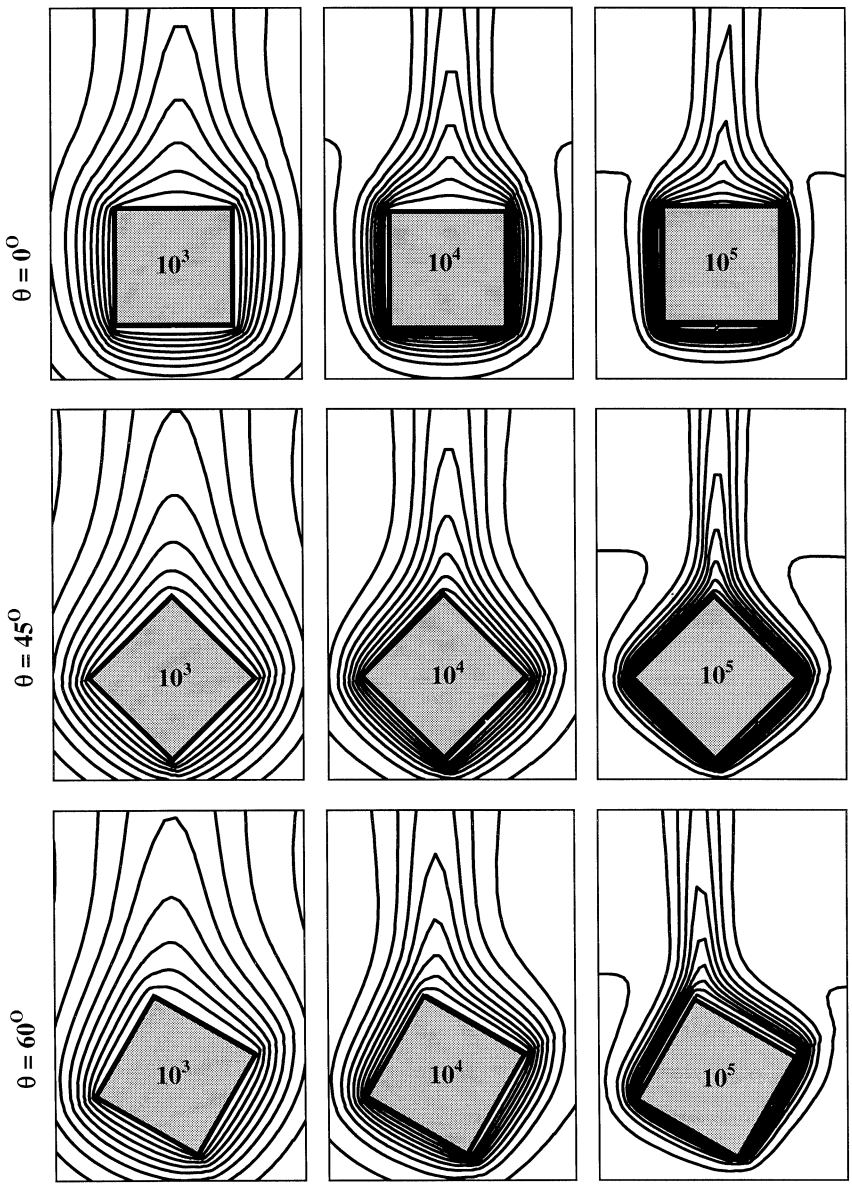

FIG. 3
Isothermal lines at different Grashof numbers and orientations

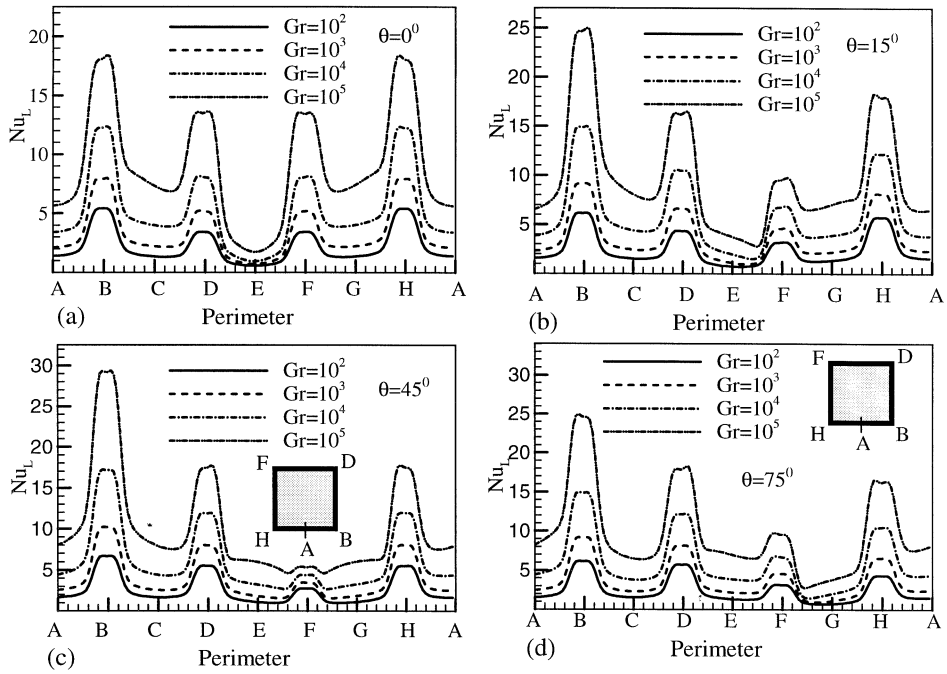

FIG. 4
Local Nusselt number distribution along the perimeter of the cylinder

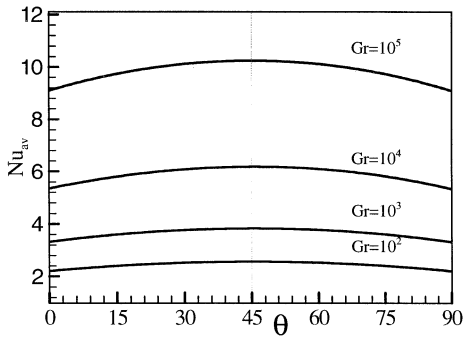

FIG. 5
Average Nusselt number as a function of θ

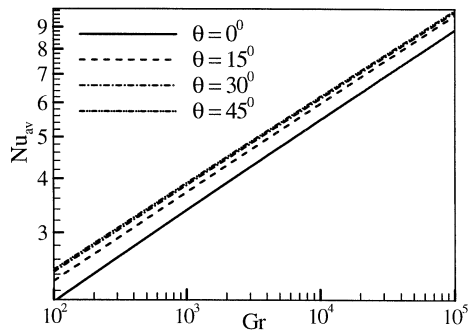

FIG. 6
Average Nusselt number as a function of Gr

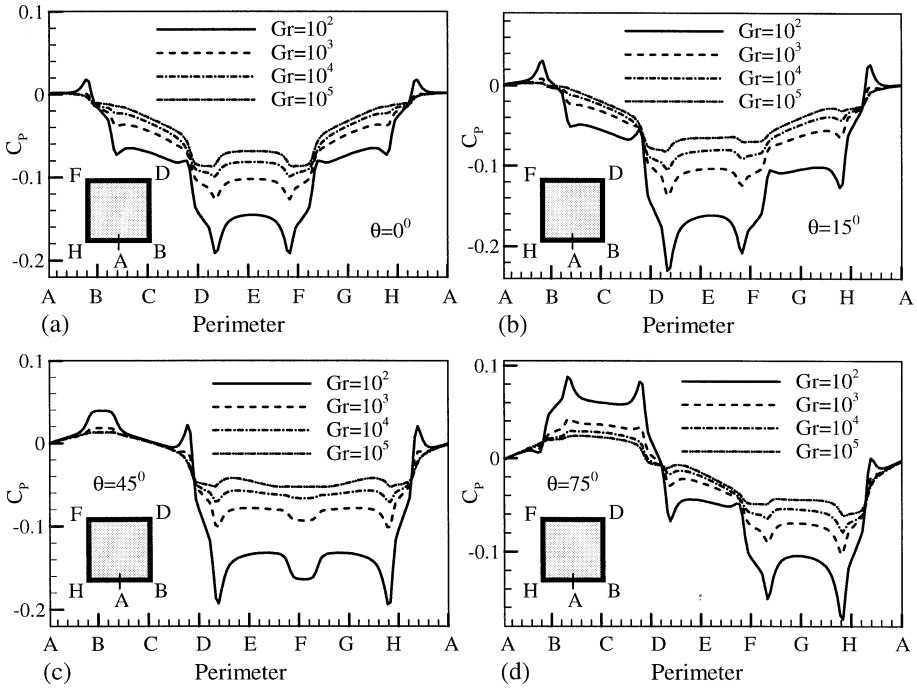

FIG. 7
Distribution of Pressure coefficient along the perimeter of the cylinder

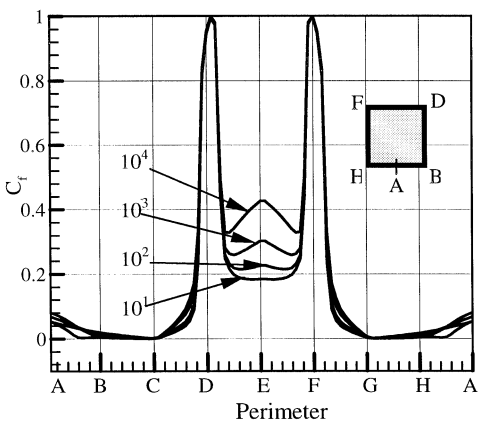

FIG. 8
Skin friction distribution

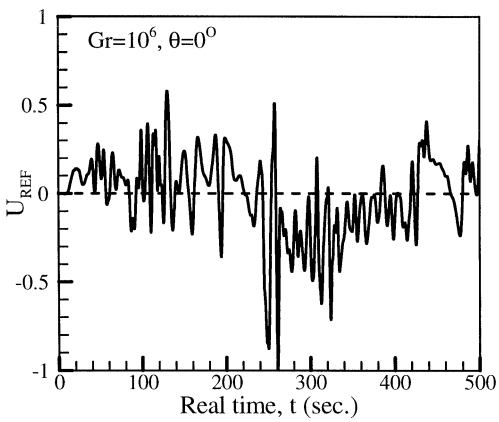

FIG. 9
Velocity fluctuation at reference location

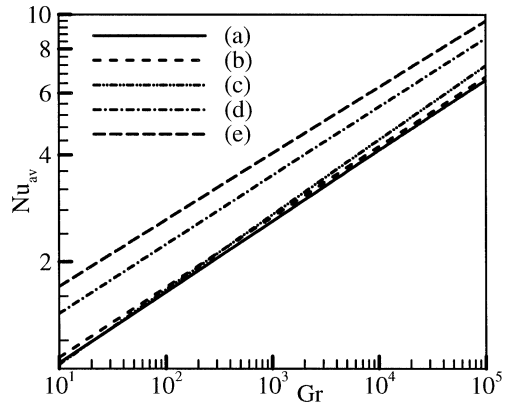

FIG. 10

Comparison of Nusselt numbers of different cylinder (a) circular, (b) ellipse with major axis horizontal, (c) ellipse with major axis vertical, (d) square cylinder at $\theta=0^0$, and (e) square cylinder at $\theta=45^0$

Pressure distribution along the cylinder perimeter is presented in the form of dimensionless pressure coefficient (C_P). Effect of Gr and orientation on C_P are shown in Figs. 7(a) – (d). C_P distribution is symmetrical at $\theta=0^0$ and 45^0 for the symmetrical obstruction of cylinder across the buoyant flow. Profiles are similar to sub-critical one if compared with the case of forced flow.

Wall shear stress is calculated in the form of skin friction coefficient (C_f) and is presented in Fig. 8. Gr shows little influence on the C_f profiles. At two upper corners (F and D), where velocity gradient is the largest, peak values of C_f are observed. Then a drastic fall occurs due to the onset of separation of buoyant plume from the upper surface of the cylinder. Only these portions of C_f profiles show Gr dependent variation.

Present work is restricted in steady-laminar case and carried out for Gr up to 10^5. The starting point of transition from laminar to turbulence is very difficult to identify and time consuming. Time marching solution has been done only for some selected Grashof numbers at $\theta=0^0$ just for observing some transitional characteristics. Fig. 9 shows the velocity variation with time at preselected reference location (3×D vertically upward from the center of the cylinder) for $Gr=10^6$. Fluctuation of reference velocity (U_{REF}) clearly indicates the flow transition.

Conclusions

We have attempted to show some of the details of flow and thermal field characteristics near a square cylinder at different orientation. In most cases, we have shown the variation of parameters like C_P, C_f, Nu_L along the perimeter of the cylinder. Average heat transfer shows its maximum value at $\theta=45^0$ compared to the same at other orientations. Flow remains steady around $Gr=10^5$. After which oscillatory flow is observed that indicates the transition to turbulence. In present study, we did not calculate the critical value of Gr that starts transition. Finally for convenience of comparison, heat transfer results of circular cylinder, elliptical cylinder with major axis horizontal and then vertical, square cylinder at $\theta=0^0$ and 45^0 are presented (Fig. 10). The surface area of each cylinder is kept constant.

Nomenclature

C_f	skin friction coefficient = $2\tau_w/(\rho U_0^2)$
C_P	pressure coefficient = $2.\Delta P/(\rho U_0^2)$
D	characteristic length = $L.(Cos\theta+Sin\theta)$
g	gravity vector, $m.sec^{-2}$
Gr	Grashof number = $\rho^2.g.\beta.\Delta T.D^3/\mu^2$
h	heat transfer coefficient, $W.m^{-2}.{}^0C^{-1}$
k_f	thermal conductivity of fluid, $W.m^{-1}.{}^0C^{-1}$
L	length of the square, m
$\dot{m}$	mass flow rate, $Kg.sec^{-1}$
n	surface normal
Nu_{av}	average Nusselt number
Nu_L	local Nusselt number = $h.D/k_f$
P_∞	ambient pressure, Pa
P_w	pressure at wall, Pa
q	heat flux, $W.m^{-2}$
Pr	Prandtl number = $\mu.c_p/k_f$
T_w	cylinder wall temperature, ^0C
ΔT	temperature difference = (T_w-T_∞)
V	volume of CV, m^3
	Greek
∞	ambient condition
β	coefficient of thermal expansion, $^0C^{-1}$

η local coordinate

ϕ dependent variable

ξ local coordinate

μ dynamic viscosity, Pa.sec

ρ fluid density, $Kg.m^{-3}$

θ angle of orientation

τ_w wall shear stress, Pa

References

1. S. Sathe and B. Sammakia, *J. Heat Transfer*, **120,** 830 (1998).

2. G. Cesini, M. Paroncini, G. Cortella, and M. Manzan, *Int. J. Heat Mass Transfer*, **42**, 1801 (1999).

3. B. Farouk and S.I. Guceri, *J. Heat Transfer*, **103**, 522 (1981).

4. T.H. Kuhen and R.J. Goldstein, *J. Heat Transfer*, **100**, 635 (1978).

5. S.H. Tasnim and S. Mahmud, Flow and thermal field behavior around an isothermal square cylinder in a large confined enclosure, *Proc. 3 rd Int. Conf. on Fluid Mech. and Heat Transfer*, BUET, Dhaka, Bangladesh, pp.212 – 217 (1999).

6. S.V. Patankar, *Numerical Heat Transfer and Fluid Flow*, 1st ed., McGraw-Hill, New York (1980).

7. J. Ferziger and M. Peric, *Computational Methods for Fluid Dynamics*, 1st ed., Springer Verlag, Berlin (1996).

8. H.M. Badar, *J. Heat Transfer*, **119**, 709 (1997).

9. H.M. Badar and K. Shamsher, *Int. J. Heat Mass Transfer*, **36**, 3593 (1993).

10. J.H. Merkin, *J. Heat Transfer*, **99**, 72 (1977).

Received May 21, 2002